

Interaction between buoyancy and diffusion-driven instabilities of propagating autocatalytic reaction fronts. II. Nonlinear simulations

J. D'Heroncourt,¹ J. H. Merkin,^{2,a)} and A. De Wit¹

¹*Nonlinear Physical Chemistry Unit and Center for Nonlinear Phenomena and Complex Systems, Faculté des Sciences, Université Libre de Bruxelles (ULB), CP 231-Campus Plaine, 1050 Brussels, Belgium*

²*Department of Applied Mathematics, University of Leeds, Leeds LS2 9JT, United Kingdom*

(Received 18 August 2008; accepted 9 January 2009; published online 17 March 2009)

The nonlinear dynamics resulting from the interplay between diffusive and buoyancy-driven Rayleigh–Taylor (RT) instabilities of autocatalytic traveling fronts are analyzed numerically for fronts ascending or descending in the gravity field and for various values of the relevant parameters, the Rayleigh numbers R_a and R_b of the reactant A and autocatalytic product B , respectively, and the ratio $D=D_B/D_A$ of the diffusion coefficients of the two key chemical species. The interaction between the coarsening dynamics characteristic of the RT instability and the fixed short wavelength dynamics of the diffusive instability leads in some parameter regimes to complex dynamics dominated by the irregular succession of birth and death of fingers. Large single convective fingers with a tip deformed by the short wavelength diffusive instability are also observed. If D is sufficiently small and the RT instability is active, the concentration of the slower diffusing species B can be convected to values above its fully reacted concentration. Experimental conditions that would allow the observation of the dynamics predicted here are described. © 2009 American Institute of Physics. [DOI: 10.1063/1.3077181]

I. INTRODUCTION

The nonlinear dynamics resulting from transverse instabilities of propagating chemical fronts have been studied both theoretically and experimentally in many situations. Typically fronts can become unstable either due to differential diffusion processes or because of buoyancy-driven instabilities. In the case of a diffusive instability, the front deforms because the reactant A involved in the autocatalytic process underlying the reaction-diffusion propagation diffuses sufficiently faster than the autocatalytic product B of the reaction. A key parameter of this instability is then the ratio of diffusion coefficients $D=D_B/D_A$ of autocatalyst B and reactant A which has to be lower than some critical value D_c for the diffusive instability to set in Refs. 1–3. In the nonlinear regime, a diffusive instability is characterized by the cellular deformation of the front as observed experimentally for both the iodate-arsenous acid⁴ (IAA) and chlorite-tetrathionate^{5–8} (CT) reactions. The pattern has a wavelength of the order of a centimeter and appears on a time scale of 2–3 h. Numerically, Horváth *et al.*¹ showed that the spatiotemporal dynamics of the diffusive instability can develop into chaos as the width of the system is increased. Malevanets *et al.*² performed a numerical study of the diffusive instability on a cubic scheme near and far from the onset of the front instability. Close to onset there is one length scale and the dynamics can be described by a Kuramoto–Sivashinsky (KS) equation while far from onset, the dynamics feature two characteristic lengths and cannot be modeled by the KS equation.²

Fronts can also become unstable through a buoyancy-

driven Rayleigh–Taylor (RT) instability occurring when a heavier solution lies above a lighter one in the gravity field. This hydrodynamic instability occurs typically much faster as fingers with a wavelength of the order of 1 millimeter appear in less than half a minute.^{9,10} In Hele–Shaw cells (two Plexiglas plates separated by a thin gap width) which are laterally sufficiently spatially extended so that several fingers can appear at onset, the nonlinear dynamics of RT fingers shows merging and a general coarsening trend toward larger wavelengths with time. Such a coarsening tendency has long been noted in viscous and density fingering in nonreactive fluids.¹¹ It has also been observed experimentally in the RT fingering of autocatalytic fronts both in the IAA reaction^{12,13} and in the CT system^{14–16} where it is seen that some slightly more advanced fingers can shield their neighbors leading to an overall decrease in the wavelength with time. In some regimes tip splitting, through which large fingers split into two smaller ones, are observed as well.^{12–16} From a numerical point of view, nonlinear simulations on both a cubic scheme modeling the IAA reaction^{17,18} and a kinetic scheme of order four modeling the CT reaction^{19,20} show coarsening toward one single asymptotic finger featuring self-similar properties.^{17,20} For large Rayleigh numbers, this coarsening trend is counterbalanced by tip splitting events.

It has been suggested recently that these two instabilities could interact if their characteristic time and spatial scales become of the same order.^{21,22} In combustion, nonlinear simulations have shown, based on a model coupling the compressible Navier–Stokes equations with energy and species conservation equations that irregular and complicated cellular flame front dynamics can result from the interaction between these instabilities.^{23–25}

^{a)}Electronic mail: amtjhm@maths.leeds.ac.uk.

In this context, it is the objective of this article to analyze numerically the spatiotemporal dynamics that result from the interaction between the diffusive and RT instabilities of autocatalytic isothermal chemical fronts. In Part I of this two paper series,²² we have set up the model equations²¹ describing the problem and undertaken a systematic linear stability analysis (LSA) to see how the interaction between diffusive and fingering modes can modify the dispersion curves with regard to the pure instabilities considered separately. Here numerical simulations of the full nonlinear model show that the predictions of the LSA (Ref. 22) are fully borne out by the dynamics of the nonlinear model at early times. Moreover, in the nonlinear regime where fingers are interacting, properties of the cellular modulation of the front are different depending on whether the pure diffusive or RT instabilities are acting alone or are interacting. Nonlinear long-time dynamics are analyzed for characteristic values of the relevant parameters, namely, D , the ratio of diffusion coefficients of the autocatalytic species B over that of the reactant A controlling the diffusive instability, and R_a and R_b , respectively, the Rayleigh numbers of the two key species A and B controlling the RT instability. We show, in particular, that, when both mechanisms of instability are cooperating to destabilize the front, the spatiotemporal dynamics of the concentrations become particularly complex.

This article is organized as follows: in Sec. II we discuss the nonlinear model we are studying and introduce the numerical scheme used to integrate the relevant equations. In Sec. III, we recall the spatiotemporal dynamics of the pure diffusive and pure RT instabilities before tackling in Secs. IV and V the dynamics resulting from their interaction. Finally some general conclusions are drawn in Sec. VI.

II. MODEL AND NUMERICAL SCHEME

Our model is based on the cubic autocatalytic reaction



where a and b are, respectively, the concentrations of reactant A and autocatalyst B and k_0 is a constant. The nonlinear dimensionless model describing reaction–diffusion–convection dynamics developing around traveling fronts generated by these kinetics is^{21,22}

$$\nabla^2 \psi = -(R_a a_y + R_b b_y), \quad (2)$$

$$a_t + \psi_y a_x - \psi_x a_y = \nabla^2 a - ab^2, \quad (3)$$

$$b_t + \psi_y b_x - \psi_x b_y = D \nabla^2 b + ab^2, \quad (4)$$

where ψ is the stream function and a and b are the concentrations of the reactant A and autocatalytic product B , respectively. The subscripts t , x , and y denote the derivative with regard to time t , longitudinal x , and transverse y spatial coordinates, respectively, with x pointing upward in the gravity field. The problem is controlled by three parameters, $D = D_B/D_A$, the ratio of diffusion coefficients of the two key species important for discussing the diffusive instability, and

the two Rayleigh numbers R_a and R_b of the reactant and product, respectively, controlling the buoyancy effects. The system is diffusively unstable for the cubic kinetics (1) if $D < D_c \approx 0.424$.^{21,22} A RT instability arises if a heavier solution lies on top of a lighter one, i.e., for ascending fronts when $R_a > R_b$, as is the case for the IAA reaction, or for descending fronts when $R_b > R_a$, as, for example, in the CT reaction.

The nonlinear simulations are performed using a numerical code based on the pseudospectral technique developed by Tan and Homsy²⁶ and adapted with previous success to tackle reactive problems.¹⁷ The simulations are started with a product zone where $(a, b) = (0, 1)$ centered around $L_x/2$ and sandwiched in a reactant zone where $(a, b) = (1, 0)$. This allows us to trigger simultaneously both an ascending and a descending front. The longitudinal extent of the product zone is chosen sufficiently wide so that the convective flows that develop on one front do not interact with the other front.²⁷ This is checked by verifying that at each time there is a zone where $\psi = 0$ between the two fronts (as is illustrated in Fig. 6 below). In effect, the dynamics of both the ascending and descending fronts remain totally independent. At the initial transition zones between a and b a random noise of 0.1% in amplitude is added to an intermediate line $a = b = 0.5$. Initially there is no flow and hence the stream function $\psi = 0$. Periodic boundary conditions are applied in both directions. We integrated the system in a two-dimensional (2D) domain of dimensionless width $L_y = 512$ and length $L_x = 8192$ and we varied the three key parameters of the problem namely D , R_a and R_b . As done in our previous LSA study^{21,22} we take the ratio R_b/R_a as fixed, namely, $R_b = 0.5R_a$ when discussing cases for which $R_a > R_b$ and $R_b = 2R_a$ for cases when $R_b > R_a$. The spatial and time discretization are respectively $dx = dy = 2$ and $dt = 0.04$.

We first tested that our nonlinear simulations correctly reproduce the predictions of the linear stability analysis. To compute the most unstable growth rates, we follow over time the longitudinally averaged concentration profiles defined as

$$\langle a(y, t) \rangle = \frac{1}{L_x} \int_0^{L_x} a(x, y, t) dx \quad (5)$$

for a , with a similar definition for b . We then Fourier transform this profile and identify the most unstable wavenumber k_{\max} as the one with the largest power A_{\max} in the Fourier spectrum. In the linear regime, the amplitude A_{\max} of the modes grow exponentially with a growth rate σ_{\max} . This growth rate of the most unstable mode is therefore obtained as the slope of a linear fit to the curve $\log(A_{\max})$ as a function of time. The related most unstable wavenumbers $k = k_{\max}$ and growth rates σ_{\max} computed using this technique show, for all values of parameters tested, good agreement with values computed by our LSA.²² This validates both the LSA and the present nonlinear simulations. Furthermore, we have checked that we correctly reproduce the most unstable wavenumber and the growth rate for the pure diffusive case as presented in Ref. 3.

The nonlinear dynamics are followed by displaying at a given time 2D concentration fields $a(x, y, t)$ or $b(x, y, t)$ in a

gray scale ranging from zero in white to the maximum value (which is equal to one unless stated otherwise) in black. The width of the plots are always $L_y=512$ while the length along x varies but can easily be found as the same scales for both x and y are kept in all 2D concentration plots. Moreover we compute transversally averaged concentration profiles defined as

$$\langle a(x,t) \rangle = \frac{1}{L_y} \int_0^{L_y} a(x,y,t) dy. \quad (6)$$

These one-dimensional profiles allow us to follow the temporal evolution of concentrations averaged over the width of the system. The spatiotemporal evolution of the dynamics of the fingers can also be followed by plotting space-time maps of the location of the maxima (in black) and of the minima (in gray) of the longitudinally averaged profiles (5).

III. DIFFUSION-DRIVEN AND RAYLEIGH-TAYLOR INSTABILITIES

Before focusing on the more complex situations due to the coupling between the buoyancy- and diffusive-driven instabilities we wish to draw the base line of the problem by recalling the nonlinear dynamics of each of the pure instabilities, namely, the diffusive instability for different values of the parameter $D < D_c$ but with $R_a=R_b=0$ and the RT instability for R_a and R_b nonzero but with $D=1$.

A. Diffusion-driven instability

For the cubic scheme considered in Eq. (1), the pure diffusive instability develops on both the ascending and descending fronts when $D < D_c \approx 0.424$ and $R_a=R_b=0$. This pure diffusive case is presented in Fig. 1 for four different values of $D < D_c$ by space-time maps of the extrema of the longitudinally averaged profile $\langle a(y,t) \rangle$. At early times, the amplitudes of the initial perturbations grow and fingers appear with a wavelength and onset time corresponding to the one predicted by the LSA.^{3,21,22} We note that this wavelength decreases with D in agreement with the fact that the system is getting more unstable (i.e., k_{\max} increases) when D is progressively decreased below the critical threshold D_c of the diffusive instability. For $D=0.4$ slightly below the critical value, a regular cellular pattern of seven fingers with fixed wavelength sets (Fig. 1, bottom right panel). If D is progressively decreased, nonlinear interactions between fingers can lead to merging phenomena whereby two neighboring fingers coalesce into one which translates in the space-time map by a line ending at one point. Counter to this, some fingers can also split into two which is seen in the space-time map by the birth of a new line. These events are rare for $D=0.3$, however, their occurrence becomes more frequent as D is further decreased (see the plots for $D=0.1, 0.2$). In all cases the deformation to the planar reaction front keeps its short amplitude and short wavelength character, as can be seen on the inset of Fig. 1 featuring a gray-level plot of the a concentration at time $t=8000$. These numerical results reproduce experimental findings obtained with the IAA (Ref. 4) and CT reaction.^{5,6} The observation that the number of space-time

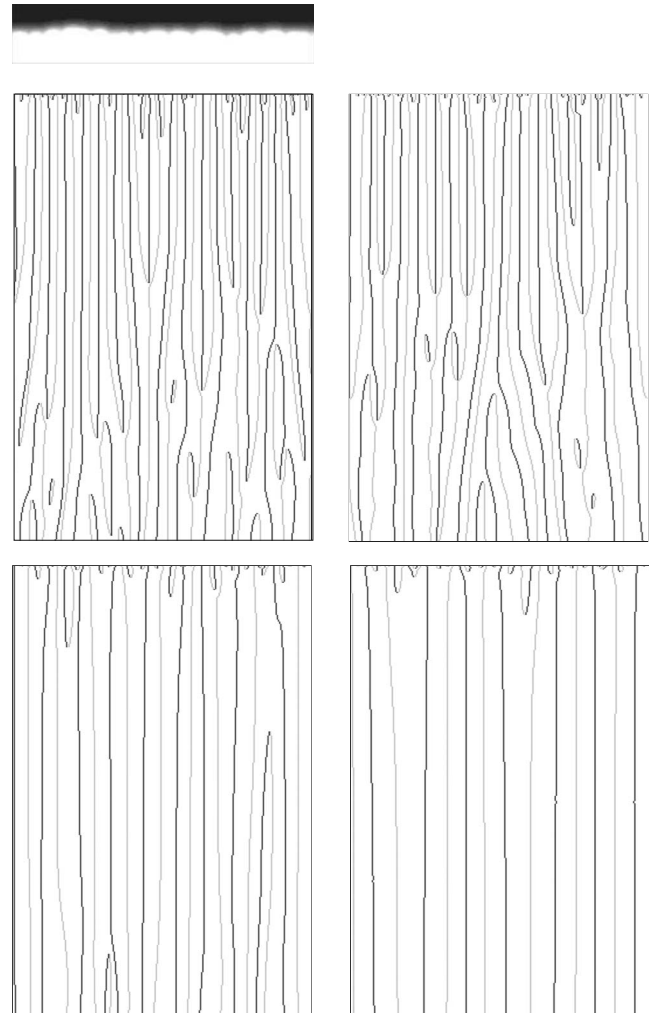


FIG. 1. Space-time map of the extrema of $\langle a(y,t) \rangle$ for the pure diffusive instability with $R_a=R_b=0$ and $D=0.1, 0.2, 0.3, 0.4$ (from left to right and top to bottom). The horizontal axis is the y direction ranging from 0 to $L_y=512$ while the vertical axis represents time from $t=0$ to $t=8000$ (t increasing in the downward direction). The inset on top shows a zoom on the front deformation by plotting the concentration of a at $t=8000$ for $D=0.1$ on a scale ranging from black ($a=1$) to white ($a=0$) with $L_x=200$, $L_y=512$.

defects associated with the birth and death of the fingers increase with decreasing D is also consistent with the fact that spatiotemporal chaos has been shown to set in for large spatial systems when the diffusivity ratio is decreased.^{1,2}

B. Rayleigh–Taylor instability

In the absence of any differential diffusion effect, i.e., for $D=1$, a pure RT instability may develop as soon as the Rayleigh numbers R_a and R_b are different. There is a range of unstable wavenumbers, dependent on R_a , where this instability is operative and domains of sufficient size to accommodate these unstable wavenumbers are required to activate an RT instability.^{27,28} Our numerical simulations are performed in spatial domains large enough to allow RT instabilities to form. When $R_a > R_b$, the upward propagating front for which heavier reactants A lie on top of lighter products B is unstable with regard to buoyancy-driven flows ($\psi \neq 0$), whereas the descending front remains stable as it features a statically stable density stratification. Figure 2 shows the

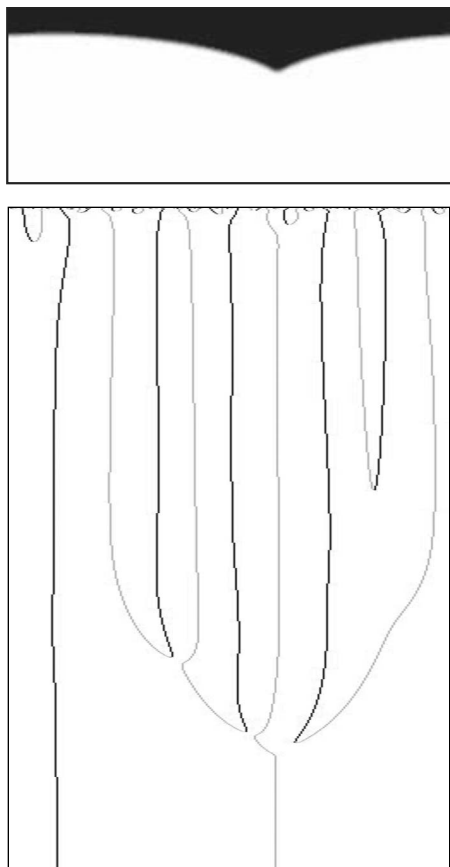


FIG. 2. Coarsening nonlinear dynamics of the pure RT instability ($R_a=0.5$, $R_b=0.25$, $D=1$). Same plot as in Fig. 1 except final time is $t=7500$.

space-time map of extrema of $\langle a(y,t) \rangle$ for the buoyantly unstable ascending front with $R_a=0.5$, $R_b=0.25$, $D=1$. After the appearance of five fingers at onset in good agreement with the LSA for these values of parameters,²² the nonlinear RT dynamics is characterized by a general coarsening trend resulting from the merging of fingers in the course of time.^{14,17} Eventually, there is only one single finger left in the system as seen on the upper part of Fig. 2. The isothermal RT fingering of fronts is known to feature tip splitting for large systems and/or large Rayleigh numbers.^{12-14,17,20} Heat losses through the walls of the reactor have also been shown to favor tip splittings.^{13,29} However, for the width L_y , the small values of the Rayleigh numbers and the isothermal conditions chosen here, no tip splitting is observed. Note that the same dynamics are obtained for a pure downward propagating front when $R_b > R_a$.

Having recalled the nonlinear dynamics of both pure diffusive and pure RT instabilities, we now examine the dynamics that are obtained when these two instabilities interact.

IV. COUPLED BUOYANCY/DIFFUSION-DRIVEN INSTABILITIES FOR $R_a > R_b$

Our LSA analysis of the problem has shown that different phenomena are to be expected depending whether $R_a > R_b$ or $R_b > R_a$. The expected trends predicted by this LSA are summarized in Table I of Ref. 22. We first analyze

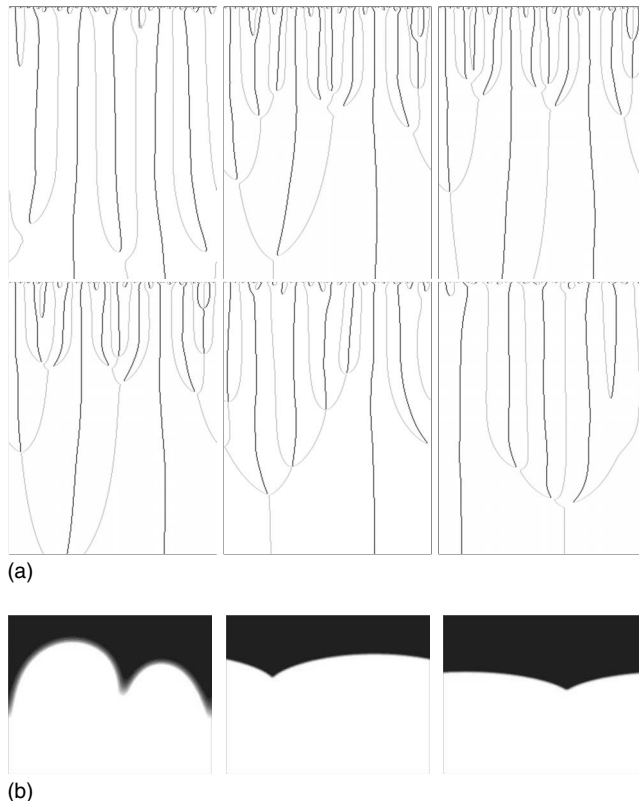


FIG. 3. Space-time maps of the extrema of $\langle a(y,t) \rangle$ for ascending fronts with $R_a=0.5$, $R_b=0.25$ from $t=0$ to $t=7000$ for $D=0.1, 0.2, 0.3, 0.4, 0.6$, and $D=1.0$ (from left to right and top to bottom). The three lower panels show from left to right the concentration a in the front at $t=7000$ for $D=0.1, 0.6, 1.0$ on a scale ranging from black ($a=1$) to white ($a=0$) with $L_x=200$, $L_y=512$.

the case $R_a > R_b$ where the reactant A is heavier than the product B and the density decreases in the course of reaction as, for example, in the IAA reaction.

A. $D > D_c$

For $D > D_c$, the system is diffusively stable and only the ascending front is buoyantly unstable, the descending one remaining planar. Our nonlinear simulations confirm this with an instability appearing only on upward propagating fronts. We illustrate this in Fig. 3 with the plots for $D=0.6, 1.0$. The initial small perturbations start to develop with wavelengths and growth rates in agreement with those of the corresponding LSA.²² These perturbations grow in amplitude and coalesce into the long wavelength single reaction finger normally associated with the pure RT case seen above. Differential diffusion is however playing a subtle effect as having $D > 1$ is stabilizing the hydrodynamic unstable modes for $R_a > R_b$ (see Fig. 3 of Ref. 22) while $D_c < D < 1$ is having a destabilizing effect (see Fig. 4 of Ref. 22). This can be checked on the space-time maps of the nonlinear simulations in Fig. 3 where the number of fingers at onset is larger for $D=0.6$ than for $D=1$ confirming that the system is more unstable at lower values of D . In the nonlinear regime, the buoyancy forces are here strong enough to retain the coarsening characteristic of the buoyancy-driven instability. However, subtle effects are at play as the coarsening is more efficient for $D=0.6$ than for $D=1.0$. This can be explained by

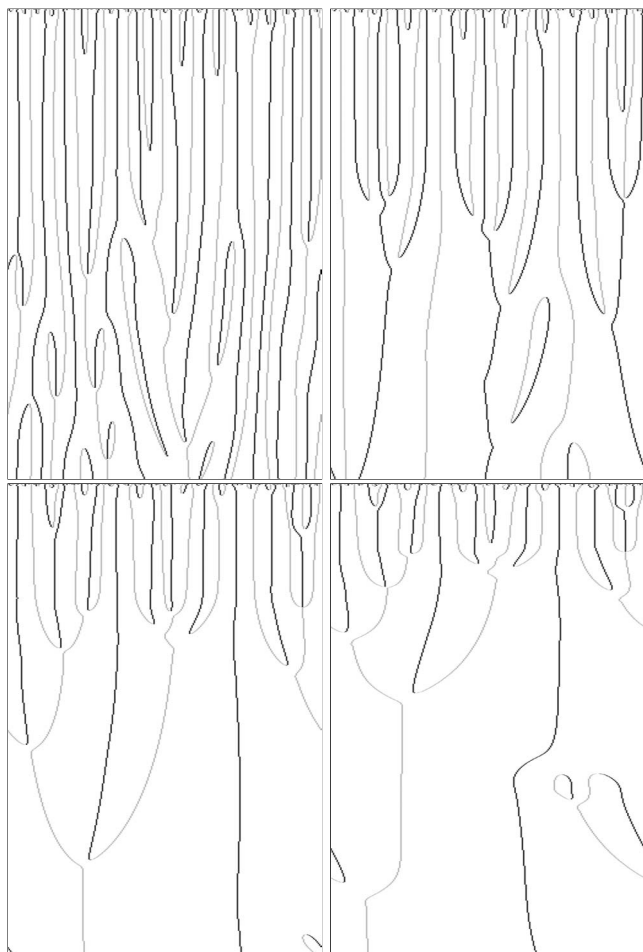


FIG. 4. Influence of the Rayleigh number on the diffusive instability shown with space-time maps of the extrema of $\langle a(y,t) \rangle$ for ascending fronts with $D=0.2$ and R_a increasing as $R_a=0.1, 0.25, 0.5, 1.0$ from left to right and top to bottom shown from $t=0$ to $t=8000$. When R_a increases, the buoyant effects become more dominant and impose a coarsening trend.

the fact that the reaction-diffusion speed of the front is decreasing with D . Thus the front propagates slower for $D=0.6$ than for $D=1$ which allows convection to be more efficient. When reaching the final single finger (lower panel of Fig. 3), the amplitude of the finger is also slightly larger for $D=0.6$ than for $D=1$.

B. $D < D_c$

When $D < D_c$ the system is also diffusively unstable and both ascending and descending fronts will feature cellular deformations. We analyze the dynamics when coupled to buoyancy-driven convection separately.

1. Ascending fronts

Figure 3 also shows space-time maps of the dynamics for $R_a > R_b$ and various values of $D < D_c$. Hence both diffusive and RT instability modes are simultaneously at play. Again the perturbations develop initially with growth rates and wavelengths consistent with those given by the LSA. The RT dynamics has a coarsening trend (see Fig. 2) while the diffusive instability features a more constant number of fingers on average (see Fig. 1). When both instabilities are

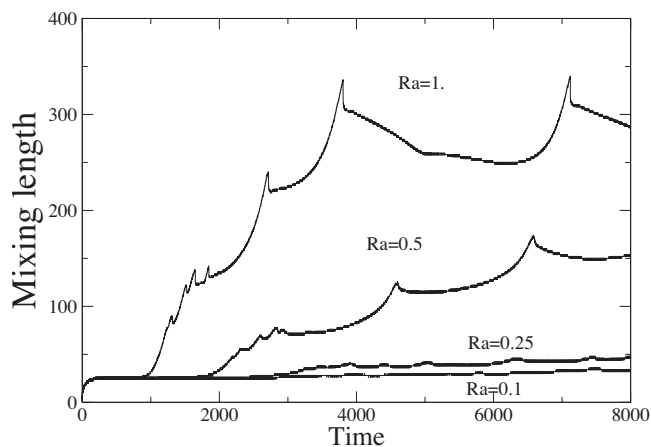


FIG. 5. Mixing length as a function of time for ascending fronts with $D=0.2$ and various values of $R_a=2R_b$.

operative, the dynamics will therefore depend on the relative weight of each instability. The smaller the value of D for a fixed set of Rayleigh numbers, the less efficient the coarsening dynamics, the more coalescence and splitting of the perturbations and the larger the amplitude of the fingers as can be seen in Fig. 3.

Similarly at a fixed $D=0.2$, the coarsening dynamics is taking over when R_a is increased as shown in Fig. 4. For $R_a=0.1$, perhaps less so for $R_a=0.25$, there is repeated coalescence and splitting of reaction fingers and the instability retains the short wavelength character of a diffusion-driven instability. For larger values of R_a , the destabilizing effect of buoyancy becomes increasingly important and coarsening takes over. There is then also increased convection strength in the system. This cannot be appreciated on space-time maps of the concentration dynamics but is better evidenced by analyzing the temporal evolution of the mixing length W (defined as the length of the zone where $\langle a(x,t) \rangle$ is larger than 0.01 and smaller than 0.99).¹⁷ The mixing length is plotted in Fig. 5 which shows that there is very little increase in the longitudinal extent of the finger from $R_a=0.1$ to $R_a=0.25$ both taking small values between 35 and 45 (in dimensionless units). However, the extent of the reaction increases considerably in going to $R_a=0.5$, approximately 150 now showing strong fluid convection, and keeps increasing for the larger values of R_a , showing the strong effects of the destabilizing influence of buoyancy which also starts earlier when R_a is increased.

Another feature which differentiates the cases for $D < D_c$ and $D > D_c$ is a difference in the concentration profiles of the two species A and B . This can be seen in Fig. 6 featuring density plots of the 2D concentration fields a and b as well as the stream function ψ . This figure shows that the convective flow is localized to a region around the reaction front. The spatial distribution of both species is similar for $D=0.6$ while the dynamics of B extends on larger scales and is more affected by convection than A for $D=0.1$. Moreover, for $D=0.1$, there are regions where the concentration of B achieves values above the fully reacted state $b=1$ that arises behind the planar reaction front. This can be seen in the $\langle b(x,t) \rangle$ plots in Fig. 7 where bumps of concentration burst-

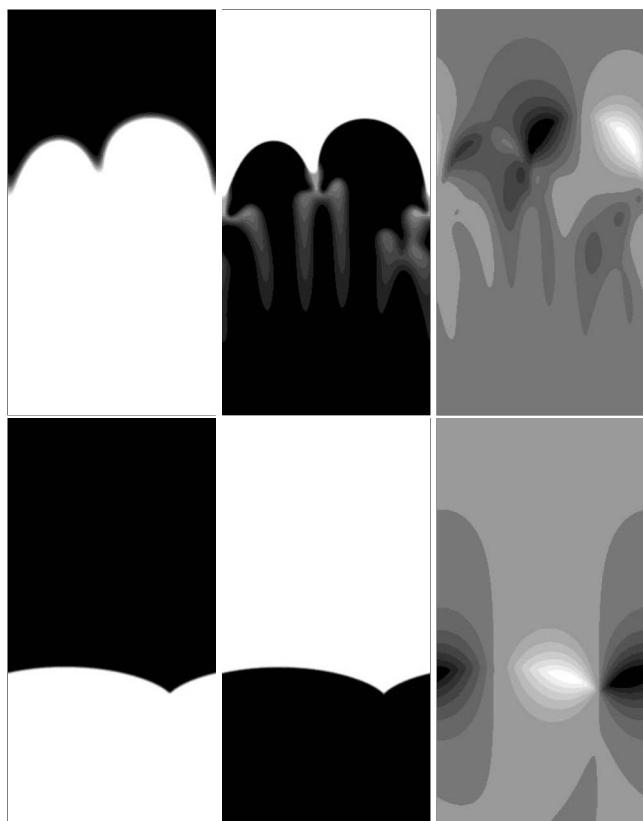


FIG. 6. Concentrations of a , b , and the stream function ψ , from left to right, for $D=0.1$ (first row) and for $D=0.6$ (second row) for $R_a=0.5$, $R_b=0.25$ shown at $t=7000$ in a zoom of size $L_x=400$, $L_y=512$ around the front.

ing over 1 and troughs where the concentration is lower than 1 are observed while a keeps ranging from 1 to 0. The fact that locally b is increased over 1 is due to a convective concentration of this species which is insufficiently balanced by its slow diffusion. This feature disappears when $D=0.6$ for which the averaged profiles of a and b both range between 0 and 1. These results show that there is a strong interaction between the local reaction and the convective flow for this case. The transport of reactant A by the convective flow enables the concentration of B to build up in some regions above the normal fully reacted state and the transport of the autocatalyst by the flow leads to its depletion in other regions. This behavior is consistent with the LSA which shows that a stronger instability should develop when $D < D_c$.

2. Descending fronts

The LSA predicts that downward propagating fronts will remain stable when $R_a > R_b$ and $D > D_c$ and this is confirmed by our nonlinear simulations. However, for $D < D_c$ the LSA suggests that, for these smaller values of D , the effects of buoyancy can make the instability stronger than in the pure diffusive case, even though the density stratification is statically stable. For instance for $R_a > R_b$ and $D=0.15$, the LSA shows that both ascending and descending fronts can become unstable, the latter having the largest growth rate (see Figs. 1 and 3 in Refs. 21 and 22).

This trend predicted by the LSA is confirmed by our nonlinear simulations: for descending fronts, differential diffusion is destabilizing the otherwise buoyantly stable front

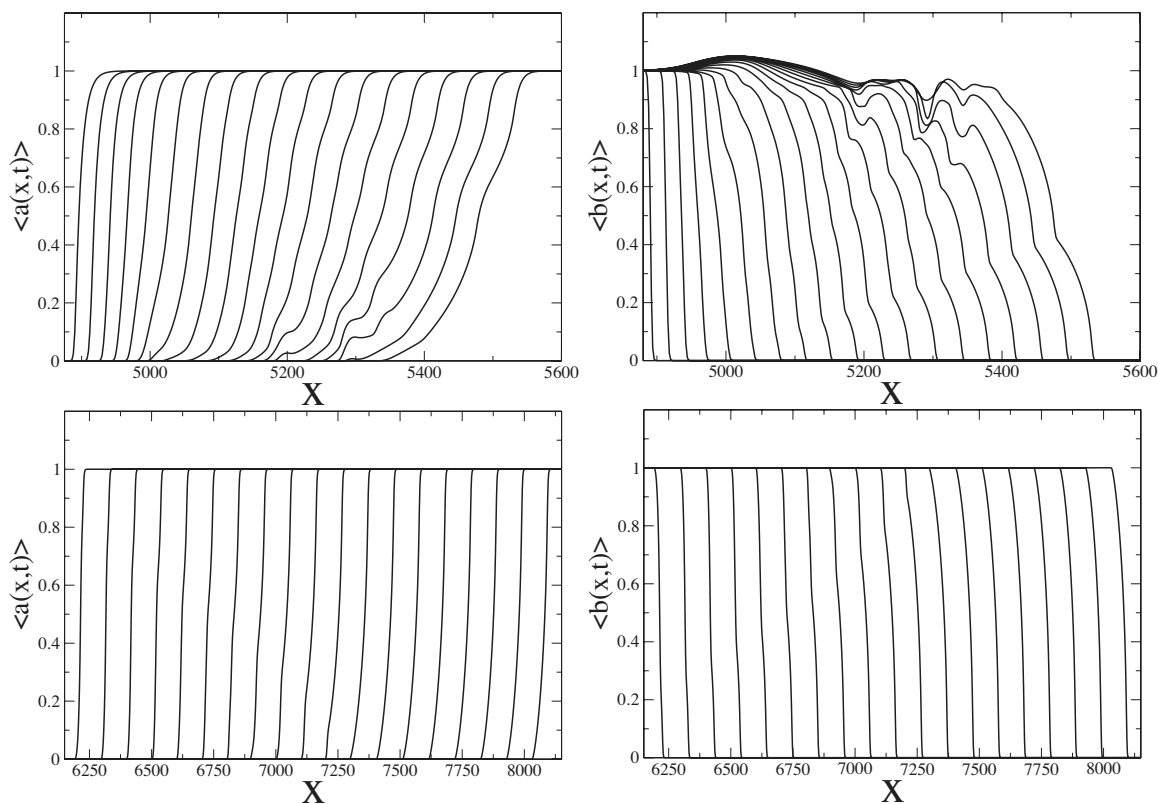


FIG. 7. Transversally averaged profiles $\langle a(x,t) \rangle$ (left) and $\langle b(x,t) \rangle$ (right) for $D=0.1$ (first line) and $D=0.6$ (second line) corresponding to the simulations of Fig. 6 from $t=3400$ to $t=7000$ with time intervals $\Delta t=200$.

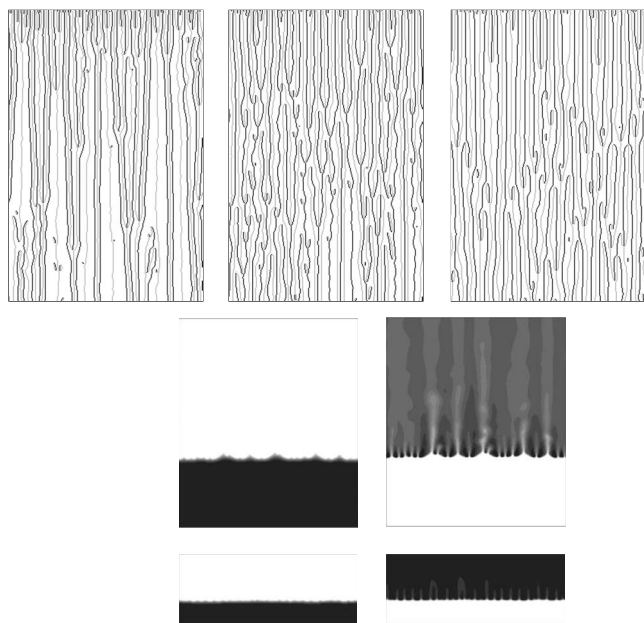


FIG. 8. Upper section: space-time maps of the extrema of $\langle a(y,t) \rangle$ for descending fronts with $R_a=0.5$, $R_b=0.25$ and $D=0.1, 0.15, 0.2$ (from left to right) from $t=0$ to $t=8000$, $L_y=512$. Lower section: concentrations of a (left column) and b (right column) for $D=0.1$ (top row) and $D=0.2$ (bottom row) at $t=8000$.

but the density difference across the front then triggers convection. The resulting nonlinear dynamics as seen in Fig. 8 (upper section) feature a smaller wavelength (larger most unstable wavenumber) than the corresponding pure diffusive cases shown in Fig. 1. There is also a clearly marked difference in character between the buoyantly unstable upward (see Fig. 3) and the downward propagating fronts (Fig. 8). Instead of the one or two long wavelength reaction fingers developing at large times on ascending fronts, no regular structures appear to develop on the downward propagating fronts. The irregular structures that do develop on the downward propagating fronts with successions of birth and deaths of fingers retain their short wavelength character, reminiscent of a diffusion-driven instability, as can be seen more clearly in Fig. 8 (lower part) where we plot the a and b concentrations. They are more pronounced with the reaction zone having a much greater lateral extent for the larger values of D and are irregular in behavior. For $D=0.1$ the plot of b shows that the convective flow gives appreciable variations in the concentration of b even at large distances behind the reaction zone having a much greater lateral extent for the larger values of D and are irregular in behavior. For $D=0.3$ and larger, we found the downward propagating fronts remained stable, consistent with the LSA, which gives a value of $D \approx 0.284$ at which stability is restored by buoyancy when $R_a=0.5$.²²

To understand this, we recall the destabilization mechanism due to the coupling between differential diffusion and buoyancy effects by considering a displaced particle argument on a downward propagating front. A perturbation ahead of the front fills in faster with heavier A than losing lighter B when $D_B < D_A$. Thus the perturbation becomes heavier than the surrounding fluid containing only A and hence continues to sink driving an instability of the otherwise buoyantly

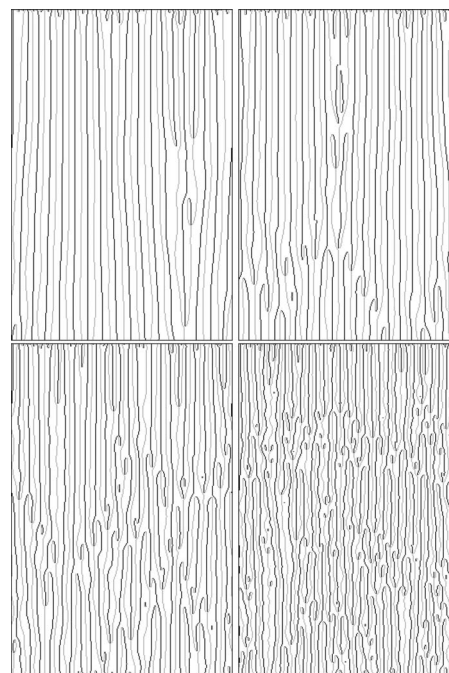


FIG. 9. Space-time maps of the extrema of $\langle a(y,t) \rangle$ for descending fronts with $D=0.2$ and $R_a=0.1, 0.25, 0.5, 1.0$ (from left to right) and $R_b=R_a/2$ from $t=0$ to $t=8000$.

stable density stratification. Similarly, a perturbation behind the front loses heavier A by diffusion faster than gaining lighter B hence the perturbation is lighter than its surroundings and can rise. This mechanism is related to solutal double-diffusive effects^{30–32} with, however, the dynamics being influenced by the diffusive instability when the density difference across the front tends to zero. It is reinforced by the fact that the RD front propagation speed c decreases with D which favors the development of buoyant flows.

The LSA also identified a value of $D \approx 0.284$ when $R_a=0.5$ above which sufficiently strong buoyancy effects can restore stability. For $D=0.3$ and larger, we find, indeed, that the downward propagating fronts remain stable, consistent with the LSA. Below this value of $D \approx 0.284$, i.e., here for a fixed value of $D=0.2$, we find that the system is more unstable when increasing R_a as seen in Fig. 9. The initial perturbations again develop with wavelengths and growth rates predicted by the LSA. For smaller values of R_a these evolve into regular, short wavelength structures indicative of a diffusion-driven instability. For these smaller values of R_a , there is only a small amount of splitting and coalescence of the perturbations. For larger values of R_a , the splitting and coalescence is much more marked and irregular behavior results as time increases. A stronger convection flow develops in this case and, as a consequence, the longitudinal extent of the reaction region is much increased.

V. COUPLED BUOYANCY/DIFFUSION-DRIVEN INSTABILITIES FOR $R_b > R_a$

If $R_b > R_a$, as in the CT reaction, for example, the density increases in the course of reaction and, in this case, it is the downward propagating fronts that are buoyantly unstable, with the upward moving fronts being stable with re-

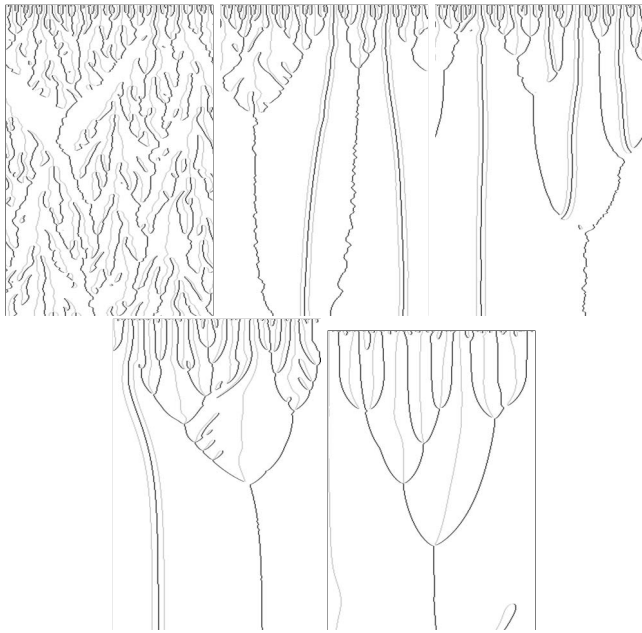


FIG. 10. Space-time maps of the extrema of $\langle a(y,t) \rangle$ for descending fronts with $R_b=0.5$, $R_a=0.25$ for $D=0.16, 0.19, 0.2, 0.4, 0.6$ (from top left to right bottom). Time is increasing downward from zero up to $t=8000$ except for the last one where $t=7700$.

gard to buoyancy-driven convection. This is what is seen in our nonlinear simulations when $D > D_c$. When $D < D_c$ the fronts are also diffusively unstable. The LSA predicts that it then requires only very small values of R_a and R_b to restore the stability of upward propagating fronts as buoyancy effects have a strong stabilizing influence on ascending fronts in this case and this is also confirmed by our simulations of the full nonlinear problem.

The coupling effects between diffusive and RT instabilities are interesting in the case of descending fronts which we now examine in detail. To do so, we plot in Fig. 10, space-time maps of the extrema of $\langle a(y,t) \rangle$ for descending fronts with $R_b=0.5$, $R_a=0.25$ for values of D increasing from $D=0.16$ to $D=0.6$. The wavelength of the perturbations seen at large times increases as D is increased. For the smaller values of D the diffusion-driven instability characteristics of small wavelength structures is retained at short times as seen when comparing the results for $D=0.16$ with those for $D=0.2$. However, for $D=0.16$ there is an irregular response, with much repeated splitting and coalescence of reaction fingers. The large time behavior that results is shown in more detail in Fig. 11 with plots of the a and b concentrations for $D=0.16$ at $t=8000$. The plot of b particularly shows that irregular structures have developed, having a large longitudinal extent. A special feature of this case is that the strong

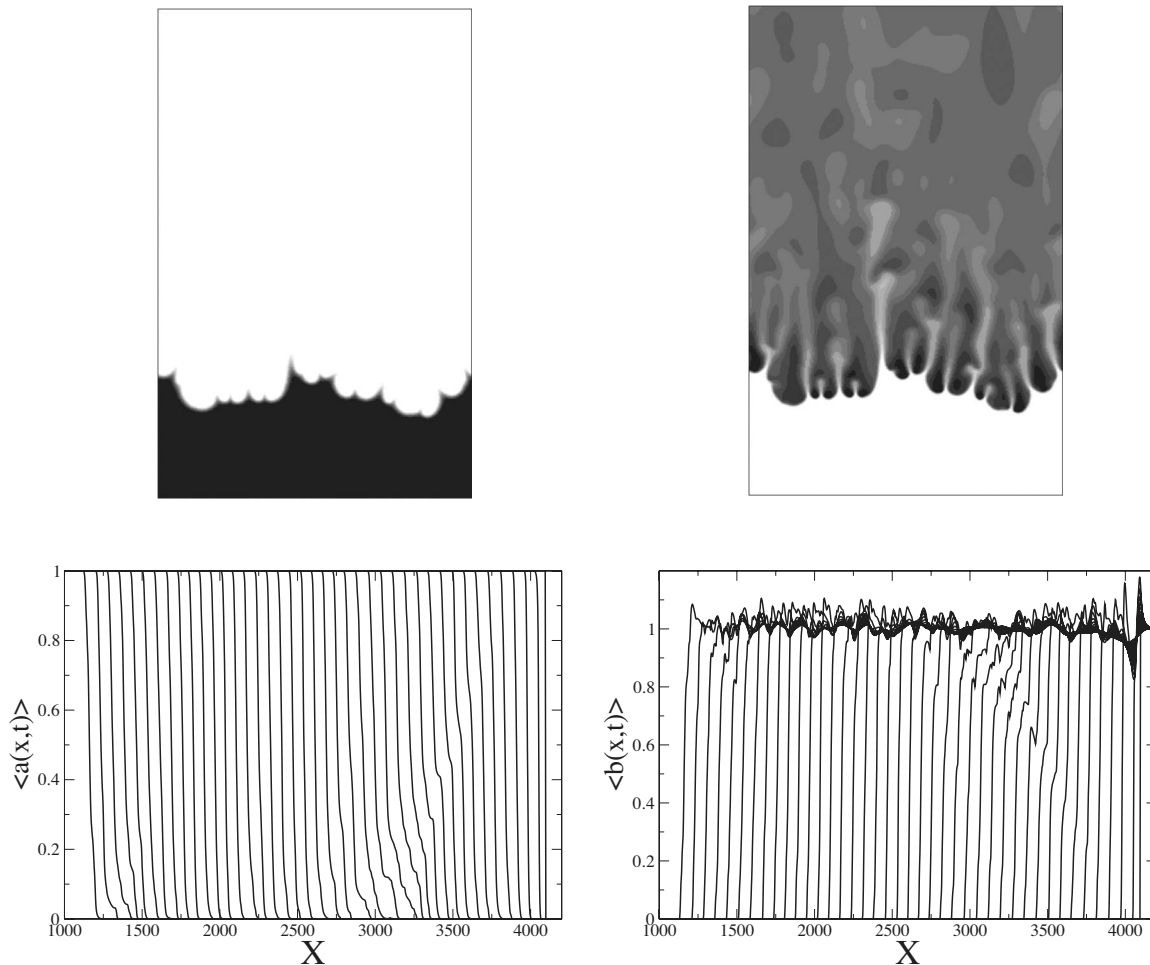


FIG. 11. Top line: concentrations of a (left) and b (right) for $R_b=0.5$, $R_a=0.25$ and $D=0.16$ taken at $t=8000$. Bottom line: the transversally averaged concentration profiles $\langle a(x,t) \rangle$ and $\langle b(x,t) \rangle$ plotted at equal time intervals.

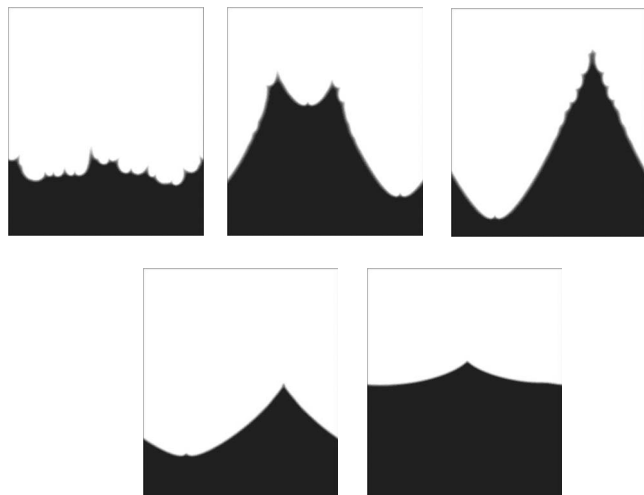


FIG. 12. Concentrations of a for the descending fronts of Fig. 10 with $R_b = 0.5$, $R_a = 0.25$ and $D = 0.16, 0.19, 0.2, 0.4, 0.6$ (top left to bottom right) shown at $t = 8000$ except in the last one for $D = 0.6$ where $t = 7000$.

convective flows can concentrate B into some regions bringing its concentration above the normally fully reacted state $b = 1$ while it can also deplete B in other regions. This is possible even though there is no A present and the reaction has terminated. This can be seen more clearly in the transversally averaged profiles of $\langle b(x, t) \rangle$ in Fig. 11.

For the larger values of D ($D = 0.4, 0.6$) in Fig. 10, the regular large wavelength finger characteristic of buoyancy-driven RT instabilities are observed at large times. There is the same general sort of behavior for $D = 0.19$ and $D = 0.2$, although now small scale structures (related to the diffusion-driven instability) appear on the larger scale reaction fingers (arising from the buoyancy-driven instability). This is manifested by small undulations appearing on the space-time maps of the maxima of $\langle a(y, t) \rangle$ in Fig. 10. The difference in behavior of the reaction front seen at large times for different values of D is made clearer in Figs. 12 and 13 where we plot a and b concentrations, respectively, at $t = 7000$. For $D = 0.16$ the front consists of small scale, irregular structures as suggested by Fig. 10. For $D = 0.19$ and $D = 0.2$ there is an obvious development of large scale reaction fingers with small scale perturbations, seen most noticeably near the apex of the reaction fingers. For $D = 0.4$ (just below D_c) this behavior has mostly disappeared, with only a small perturbation near the front of the interface, and for $D = 0.6$ ($> D_c$) only the buoyancy-driven instability is operative.

A possible explanation for the appearance of small scale disturbances on the much larger reaction fingers is that these large reaction fingers, as they develop, set up a propagating reaction front that is almost planar over length scales large compared to the much smaller length scales associated with the diffusion-driven instability. Our LSA gives $k \approx 0.2$, $\lambda \approx 30$ for the maximum growth rate of the diffusion-driven instability for $D = 0.15$, whereas the reaction fingers have a length scale approximately the width of the computational domain, $L_y = 512$. As the direction of propagation of the reaction front is not important for diffusion-driven instabilities, these RT fingers can then act as a sort of base state for the initiation of small scale diffusion-driven instabilities caused

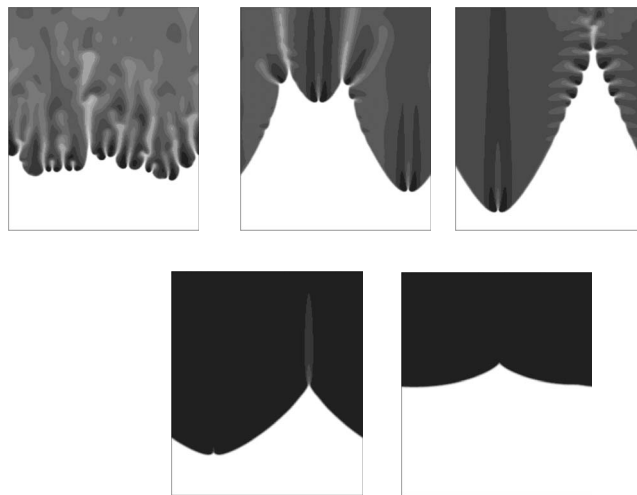


FIG. 13. Same as for Fig. 12 but for the concentration of b . [In this figure the scale in the x (vertical) direction has been elongated slightly to enable the variations in the concentration of B to be more easily seen.]

by slight perturbations that arise on them if $D < D_c$. This can be seen in the a, b concentration plots for $D = 0.19$ and $D = 0.2$ in Figs. 12 and 13. For the smaller values of D ($D = 0.16, 0.19, 0.2$), the convection resulting from changes in density across the reaction zone gives considerable variations in the concentration of b in a region well behind where the reaction takes place.

VI. CONCLUSIONS

The interaction between diffusive and RT instabilities of autocatalytic propagating fronts can affect the stability and nonlinear dynamics of the system. Here we have analyzed by nonlinear simulations the long-time dynamics resulting from such interactions. If the density decreases in the course of the reaction ($R_a > R_b$) as in the IAA system, for example, then ascending fronts are genuinely RT unstable while descending fronts are buoyantly stable. When differential diffusion comes into play, we find for ascending fronts a transition between a coarsening dynamics typical of RT modes toward a smaller wavelength diffusive instability mode when D is progressively decreased. Descending fronts are seen to be much more unstable when both modes interact with a small wavelength pattern undergoing the complex dynamics of repeated birth and death of fingers.

If, on the contrary, the density increases in the course of reaction ($R_b > R_a$) as in the CT system, for example, then ascending fronts are RT stable and for these buoyancy effects are able to stabilize diffusively unstable ascending fronts even if relatively weak. Both convective and diffusive modes are, however, destabilizing in the case of descending fronts which feature complex spatiotemporal dynamics for low values of $D < D_c$. Large single convective fingers with a tip deformed by the short wavelength diffusive instability are observed for D smaller but close to D_c . Interestingly, the coupling of differential diffusion and buoyancy effects enables in some cases the dynamics of the two species A and B to develop on different length scales for which the concen-

tration of the slower diffusing species B has been observed to be convected in some regions above the fully reacted concentration $b=1$ of the planar wave.

We finally discuss experimental conditions necessary to study the various dispersion curves studied in Part I (Ref. 22) and the nonlinear dynamics presented here. Since the two instabilities act on very different time scales of the order of minutes for the buoyancy-driven one and of the order of hours for the diffusive one, the key to observing the interaction is to bring them back onto the same time scale. Experimental demonstrations of the predicted instability scenarios and dynamics could be tested using, for example, the autocatalytic IAA (Refs. 1, 9, and 12) or the CT (Refs. 6 and 10) reactions. Both reactions have been used previously to study separately cellular deformations due to diffusive instabilities in gels^{1,4} where huge molecules were used to slow down the autocatalytic species and to increase the diffusivity difference between the two key species. Fingering in these chemical systems in vertical Hele–Shaw cells has been extensively studied^{9,10,12,14–16,21} and ways to decrease the strength of the instability have been presented in Refs. 10, 14, and 15. In the first¹⁰ the cell is inclined toward the horizontal to reduce the strength of convection while in the second¹⁵ the viscosity of the solution is varied resulting in a convection slow down when increased. Precise experimental conditions will depend on the autocatalytic reaction chosen. However, to fix ideas, we recall that, for the IAA system, the cubic scheme (1) is applicable which gives $D_c=0.42$ for the model we are using here. To achieve such small values for D , we propose to analyze the instability dynamics in the presence of large molecules binding the activator to obtain $D < D_c$ in aqueous solutions as done previously in experimental studies of diffusive instabilities of IAA systems in gels.⁴ Instead of using gels suppressing any convective motion, the reactive system should be contained in a Hele–Shaw inclined to the horizontal or containing a chemically inert viscous solute. This would slow down the buoyant flows to bring their characteristic time scales down to those necessary for them to interact with the diffusive modes. As solutal Rayleigh numbers are of the order of 3.8 for the IAA system³³ in vertical Hele–Shaw cells of gap width $h_0=1$ mm, we need to decrease these values roughly by a factor 10 to bring them into the range of $R_a \sim 0.5$ used here. As we have^{10,22} $R_a \sim Kg \cos \theta$ where θ is the angle made with the vertical and the permeability K of a Hele–Shaw cell of gap width h_0 is equal to $K=h_0^2/12$, this can be done by either decreasing h_0 by a factor $\sqrt{10}$ or by inclining the cell at an angle $\theta \approx \cos^{-1}(0.1)$ to the vertical, or by a combination of both.

From a theoretical point of view, an interesting perspec-

tive would be to study the onset of the complex splitting dynamics, in order to catch the complexity and try to connect this study to the one performed on the pure diffusive instability and known to feature spatiotemporal chaos.²

ACKNOWLEDGMENTS

A.D.W. thanks A. Tóth and D. Horváth for fruitful discussions and acknowledges financial support from the FNRS, Prodex and the Communauté française de Belgique (ARC program). J.D. benefitted from a FRIA Ph.D. fellowship.

- ¹D. Horváth, V. Petrov, S. K. Scott, and K. Showalter, *J. Chem. Phys.* **98**, 6332 (1993).
- ²A. Malevanets, A. Careta, and R. Kapral, *Phys. Rev. E* **52**, 4724 (1995).
- ³J. H. Merkin and I. Z. Kiss, *Phys. Rev. E* **72**, 026219 (2005).
- ⁴D. Horváth and K. Showalter, *J. Chem. Phys.* **102**, 2471 (1995).
- ⁵A. Tóth, I. Lagzi, and D. Horváth, *J. Phys. Chem.* **100**, 14837 (1996).
- ⁶D. Horváth and A. Tóth, *J. Chem. Phys.* **102**, 2471 (1995).
- ⁷A. Tóth, B. Veisz, and D. Horváth, *J. Phys. Chem. A* **102**, 5157 (1998).
- ⁸M. Fuentes, M. N. Kuperman, and P. De Kepper, *J. Phys. Chem. A* **105**, 6769 (2001).
- ⁹M. Böckmann and S. C. Müller, *Phys. Rev. Lett.* **85**, 2506 (2000).
- ¹⁰D. Horváth, T. Bánsági, Jr., and A. Tóth, *J. Chem. Phys.* **117**, 4399 (2002).
- ¹¹G. M. Homsy, *Annu. Rev. Fluid Mech.* **19**, 271 (1987).
- ¹²M. Böckmann and S. C. Müller, *Phys. Rev. E* **70**, 046302 (2004).
- ¹³L. Sebestikova, J. D'Heroncourt, M. J. B. Hauser, S. C. Müller, and A. De Wit, *Phys. Rev. E* **75**, 026309 (2007).
- ¹⁴T. Bánsági, Jr., D. Horváth, and Á. Tóth, *J. Chem. Phys.* **121**, 11912 (2004).
- ¹⁵T. Rica, D. Horváth, and Á. Tóth, *Chem. Phys. Lett.* **408**, 422 (2005).
- ¹⁶T. Tóth, D. Horváth, and Á. Tóth, *Chem. Phys. Lett.* **442**, 289 (2007).
- ¹⁷A. De Wit, *Phys. Fluids* **16**, 163 (2004).
- ¹⁸D. Lima, W. van Saarloos, and A. De Wit, *Physica D* **218**, 158 (2006).
- ¹⁹J. Yang, A. D'Onofrio, S. Kalliadasis, and A. De Wit, *J. Chem. Phys.* **117**, 9395 (2002).
- ²⁰D. Lima, A. D'Onofrio, and A. De Wit, *J. Chem. Phys.* **124**, 014509 (2006).
- ²¹J. D'Heroncourt, J. H. Merkin, and A. De Wit, *Phys. Rev. E* **76**, 035301(R) (2007).
- ²²J. D'Heroncourt, J. H. Merkin, and A. De Wit, *J. Chem. Phys.* **130**, 114502 (2009).
- ²³S. Kadowaki, *Combust. Flame* **143**, 174 (2005).
- ²⁴J. Yuan, Y. Ju, and C. K. Law, *Phys. Fluids* **17**, 074106 (2005).
- ²⁵J. Yuan, Y. Ju, and C. K. Law, *Combust. Flame* **144**, 386 (2006).
- ²⁶C. T. Tan and G. M. Homsy, *Phys. Fluids* **31**, 1330 (1988).
- ²⁷Y. Wu, D. A. Vasquez, B. F. Edwards, and J. W. Wilder, *Phys. Rev. E* **51**, 1119 (1995).
- ²⁸D. A. Vasquez, J. W. Wilder, and B. F. Edwards, *J. Chem. Phys.* **104**, 9926 (1996).
- ²⁹J. D'Heroncourt, S. Kalliadasis, and A. De Wit, *J. Chem. Phys.* **123**, 234503 (2005).
- ³⁰I. P. Nagy, A. Keresztessy, J. A. Pojman, G. Bazsa, and Z. Noszticzius, *J. Phys. Chem.* **98**, 6030 (1994).
- ³¹S. E. Pringle and R. J. Glass, *J. Fluid Mech.* **462**, 161 (2002).
- ³²J. A. Pojman and I. R. Epstein, *J. Phys. Chem.* **94**, 4966 (1990).
- ³³J. D'Heroncourt, A. Zebib, and A. De Wit, *Phys. Rev. Lett.* **96**, 154501 (2006).